# Synthesis strategies of iron nitrides at carbon cloth as battery-like electrode for hybrid supercapacitors

Karolina Kordek-Khalil[†], Adam Moyseowicz[†] and Agata K. Moyseowicz*

Department of Process Engineering and Technology of Polymer and Carbon Materials, Wrocław University of Science and Technology, Wrocław, Poland

In recent years, hybrid supercapacitors (HSCs) or supercapatteries which combine a capacitor-type electrode with an electrode based on materials exhibiting a Faradaic (battery-like) response have been intensively investigated for next-generation energy storage applications. HSCs attracted great attention due to a significant increase of maximum energy density stored while providing stable long-term performance and good rate capability. However, the electrochemical performance of the device is closely related to the inherent properties of the electrode material, including morphology and structure. In this paper, we present synthesis protocols for iron oxide/hydrophilic carbon cloth ($Fe_2O_3$@hCC) composite electrodes and their electrochemical performance as a negative electrode operating in an alkaline electrolyte. Two environmentally friendly, scalable and facile synthesis approaches were applied, including hydrothermal treatment and direct electrodeposition. Next, the $Fe_2O_3$@hCC electrodes were treated to convert iron oxide to iron nitride ($Fe_2N$). The results showed that the synthesis of the precursor for iron nitride has a direct impact on morphology, crystalline structure and electrochemical performance. Furthermore, the amorphous $Fe_2N$ obtained from electrodeposition exhibited significantly better Faradaic behavior, achieving a specific capacity up to 186 mAh g$^{-1}$, 66% higher than the composite electrode with $Fe_2N$ from the hydrothermal approach.

KEYWORDS

iron nitride, carbon cloth, electrochemical energy storage, supercapacitor, hydrothermal synthesis, electrodeposition

## 1 Introduction

The growing demand for clean and sustainable energy sources on a global scale has induced significant research efforts in the field of electrochemical energy storage. Simultaneously required are advances in energy conversion devices and the development of efficient and multipurpose energy storage solutions for the ubiquitous adoption of renewable energy systems, electric transportation, and smart grid integration. Batteries and supercapacitors play a crucial role in the efficient capture, storage, and delivery of electrical energy on demand (Yadlapalli et al., 2022). They provide an essential connection between intermittent energy sources, such as solar and wind, and the constant power demands of contemporary society.

As a result, a great deal of focus has been placed on the development of supercapacitor electrode materials to improve energy storage performance and meet the high demand for modern electronic devices. Electrode materials based on transition metal compounds, such as metal oxides, metal hydroxides, metal sulfides, and metal nitrides, are regarded as optimal for highly efficient electrochemical capacitors and hybrid supercapacitors (HSCs) (Zhi et al., 2013; Augustyn et al., 2014; Chi et al., 2018; Moyseowicz, 2019). Transition metal nitrides have the ability to substitute standard materials in a variety of applications, including electrical devices, gas sensing, ceramics, and environmental remediation. Due to their low density, large surface area, electrical properties, enhanced chemical activity, and high conductivity, nanoparticles with diverse morphologies and structures have recently attracted the interest of researchers (Zhou et al., 2019; Idrees et al., 2021). Nevertheless, similar to other conversion-type materials, obstacles such as repeated volume variation, a highly air-sensitive surface, and simple oxidation significantly degrade their properties (Adalati et al., 2022). Among the various metal nitrides, $Fe_2N$ is a very promising electroactive material because of its high electrical conductivity, low cost, easy preparation and environmental friendliness, however, limited amount of publications on its application in energy storage devices (Xu et al., 2017; Śliwak et al., 2017; Feng et al., 2023; Zhao et al., 2023).

The choice of iron is primarily motivated by its remarkable electrochemical capabilities and its abundance in nature, making it an economically feasible choice. Iron exhibits many valence states, such as $Fe^0$, $Fe^{2+}$, $Fe^{3+}$, etc., and possesses a diverse range of redox chemistry (Feng et al., 2023). These characteristics contribute to its ability to achieve high specific capacitance values. The majority of transition metal oxides/hydroxides are commonly utilized as positive electrodes, but iron oxides/hydroxides/nitrides exhibit a stable and extensive operating range in the negative potential. This characteristic renders them highly promising as negative electrodes for asymmetric or hybrid supecapacitors (Zhang et al., 2016).

Carbon materials are extensively employed in energy storage devices, particularly in electric double-layer capacitors (EDLCs) (Borenstein et al., 2017). Carbon-based materials are a very interesting group in materials science for their superior mechanical strength, structural stability, and electrical conductivity, while also being lightweight and cost-effective (Moyseowicz et al., 2021). Furthermore, carbon cloth, which is a crisscrossed interweaving structure of carbon threads that are composed of carbon fibers or nanofibers, is the most widely used current collector in the field of supercapacitors, particularly flexible supercapacitors (Chen et al., 2018). They increase the surface area of the electrodes and offer flexibility (Gong et al., 2021).

Current research on supercapacitors indicates that new strategies must be implemented to achieve comparable energy density to lithium-ion batteries. Consequently, a new strategic design for HSCs has been developed (Jin et al., 2008; Dubal et al., 2015; Moyseowicz and Moyseowicz, 2021). In such a device, the electrode configuration consists of one capacitive or pseudo-capacitive electrode and one battery-type electrode. By combining the benefits of supercapacitor and battery electrodes, this type of electrode configuration in supercapacitors makes it possible to get high energy and power densities (Cherusseri et al.,

2019). HSCs employing battery electrodes can bridge the divide between standard supercapacitors and lithium-ion batteries.

In the present study, we investigated the influence of the synthesis procedure on the morphology, crystalline structure, and electrochemical performance of $Fe_2O_3$ deposited on the carbon cloth substrate and their iron nitride analogues. Two environmentally friendly, scalable, and straightforward synthesis methods, including hydrothermal treatment and direct electrodeposition, were utilized. The results show that the precursor synthesis for iron nitride has a direct effect on the iron-based nanoparticle coating properties, which greatly impacts the electrode electrochemical behavior in a $6 \text{ mol L}^{-1}$ KOH electrolyte. The binder-less electrodes prepared from the direct electrodeposition method displayed much superior Faradaic behavior, yielding a specific capacity of up to 186 mAh $g^{-1}$, greater than the composite electrode containing $Fe_2N$ from the hydrothermal method.

# 2 Experimental section

## 2.1 Hydrophilic carbon cloth preparation

Carbon fiber cloth, supplied by the FuelCellStore, was used as a substrate for the deposition of iron oxides. Before any treatment, the commercial carbon cloth (CC) was cut into $2 \times 1 \text{ cm}^2$ pieces and washed sequentially in acetone, isopropanol and water. Its surface was oxidized by the procedure applied in other study (Kordek et al., 2019). Pieces of carbon cloth were placed in an alumina crucible and calcined in an air atmosphere at 500°C for 2 h. The obtained material was labelled hCC (hydrophilic carbon cloth).

## 2.2 Synthesis of $Fe_2O_3$ nanostructures on carbon cloth

### 2.2.1 Hydrothermal precipitation

All the chemical reagents in this experiment were used as received without any further purification. The synthesis of $Fe_2O_3$ was performed in a stainless steel autoclave using a hydrothermal approach. Firstly, a 3 mL of $2.5 \text{ mM mL}^{-1}$ of $Fe(NO_3)_3$ aqueous solution to yield was dissolved in 200 mL Mili-Q water on the magnetic stirrer. Then, the solution was placed into the stainless-steel autoclave and finally 5 mL of 10% ammonia solution was dropped. Hydrothermal treatment was performed at 180°C for 6 h. After the reaction, the autoclave was allowed to cool down to a room temperature. The obtained product was centrifuged and washed with Milli-Q water several times and dried in a vacuum oven at 60°C for 24 h.

$Fe_2O_3$ from hydrothermal synthesis was deposited on a hCC using drop-casting technique. $Fe_2O_3$-HT was dispersed in acetone using an ultrasonic bath for 30 min. The suspension of $Fe_2O_3$ was dropped into the hCC surface to obtain binder-free electrode with the 20 wt.% amount $Fe_2O_3$. Finally, the $Fe_2O_3@hCC$-HT was dried until the acetone completely evaporated.

### 2.2.2 Electrochemical deposition

The $Fe_2O_3$ films were plated on pieces of hCC by cathodic electrodeposition. Piece of carbon cloth was immersed in

electroplating bath composed of 20 mM $Fe(NO_3)_3$ aqueous solution and connected as working electrode in a standard three-electrode setup with Ag/AgCl as a reference and graphite rod as a counter electrode. A cathodic potential of −1.4 V vs. Ag/AgCl was supplied to the working electrode for 3 h. After the deposition, the sample labelled $Fe_2O_3$@hCC-E was washed thoroughly with water and dried at the temperature of 60°C overnight. The increase in the mass of the carbon cloth after electrodeposition of $Fe_2O_3$ was 20.2 wt%.

## 2.3 Preparation of the $Fe_2N$ nanostructures at carbon cloth

The resultant products ($Fe_2O_3$@hCC-E and $Fe_2O_3$@hCC-HT) were introduced in the bottom of a quartz boat and inserted into the center of a horizontal reactor. The reactor was heated up to 700 °C in the nitrogen flow of 9 L h$^{-1}$ with a heating rate of 10 ° min$^{-1}$. Afterwards, the ammonia (9 L h$^{-1}$) was introduced into the reactor for 2 h at the targeted temperature. Then, the reactor was cooled down to a room temperature under a nitrogen flow. The $Fe_2N$@hCC samples were kept under inert atmosphere before their application in the electrochemical system.

## 2.4 Structural and chemical characterization

The morphologies of iron compounds on carbon cloth were analyzed by field-emission scanning electron microscopy (FESEM, Merlin Zeiss) with an accelerating voltage of 3 kV. The structural characteristics of iron compounds on carbon cloth were revealed X-ray diffraction (XRD), performed with an Ultima IV Rigaku diffractometer using a Cu Ka2 radiation source ($\lambda$ = 1.54056 Å) and high resolution transmission electron microscopy (HRTEM, FEI Titan G3). The chemical compositions of iron oxides and nitrides on carbon cloth were determined by X-ray photoelectron spectroscopy (XPS) using a PHI 5000 VersaProbe (ULVAC-PHI) spectrometer.

## 2.5 Electrochemical measurements

The binder-free electrodes were cut out of carbon cloth with iron-based coating in the form of pellets with a geometric surface area of 0.64 cm$^2$. For electrochemical measurements, a three-electrode configuration was assembled in a Swagelok system. The measurements were performed in a 6 mol L$^{-1}$ KOH aqueous solution using gold current collectors to avoid corrosion and to preserve comparable experimental conditions. Measurements were conducted with a potentiostat–galvanostat VSP Biologic in a voltage range of −1.1÷0 V with a pitch-based activated carbon counter electrode and a mercury oxide reference electrode. The electrochemical properties of iron-based samples were determined by cyclic voltammetry at a voltage scan rate of 1–100 mV s$^{-1}$ and galvanostatic charge-discharge at current densities in the range 0.5–10 A g$^{-1}$ and EIS measurements were recorded under an open circuit potential in the frequency range of 200 kHz to 10 mHz. The specific capacity was expressed in mAh per mass of active material in one electrode. The specific capacity values

($Qs$/mAh g$^{-1}$) were calculated from the cyclic voltammetry curves and galvanostatic discharge profiles using Eqs 1, 2, respectively.

$$Q_s = \frac{\int IdV}{3.6vm_{el}} \quad (1)$$

$$Q_s = \frac{I\Delta t}{3.6m_{el}} \quad (2)$$

where I is the current (A), $\Delta t$ is the discharge time (s), $v$ is the scan rate (V s$^{-1}$), and $m_{el}$ is the mass of the active material in the electrode (g).

For the electrochemically active surface area, electrodes were measured in the non-faradaic potential region. The measurements were performed in an three-neck electrochemical cell filled with 6 mol L$^{-1}$ KOH as an electrolyte in a standard 3-electrode system. 1 cm × 1 cm pieces of carbon cloth with deposited Fe-based material and held by a Pt clip were used directly as working electrodes, while Hg|HgO electrode was used as a reference and a graphite rod as a counter electrode. The capacitive currents were derived from cyclic voltammetry plots acquired in a potential window between −0.1 and 0.1 V vs. Hg|HgO at different scan rates.

## 3 Results and discussion

In Figure 1 the comparison between the morphologies of the iron-based films deposited by the two techniques, namely from electrodeposition and hydrothermal/drop casting technique is presented, both before and after nitridation. Comparison between Figures 1A, B show the distinct difference between $Fe_2O_3$ obtained by the two methods. As can be seen, the morphology of the electrodeposited film is composed of continuously interconnected nanosheets, while hydrothermal technique led to formation of the film in the form of rather uniform nanoparticles. Partially uncovered carbon cloth surfaces also suggests that the deposition of $Fe_2O_3$ on the substrate is not homogeneous within the sample.

Figure 1C reveals that thermal treatment of the $Fe_2O_3$@hCC-E sample in an ammonia atmosphere resulted in a radical change in the film morphology. As can be seen, a porous interconnected structure was converted into polydisperse micro- and nanoparticles evenly distributed on the carbon cloth surface. On the other hand, the thermal conversion of $Fe_2O_3$@hCC-HT in ammonia resulted in the aggregation of nanoparticles and formation of bulk particles (Figure 1D). As can be seen, the nitridation procedure, even if it is performed under the identical conditions, had a very different effect on two oxide materials and the morphology of nitride samples obtained by the two techniques is also distinctly different.

Furthermore, XRD diffraction patterns (Figure 2) present very different structures for the obtained samples. As can be seen, the iron oxide sample obtained by the hydrothermal technique shows a typical pattern characteristic for hematite ($\alpha$-$Fe_2O_3$—JCPDS 33–0664) phase with reflexes located at 2Θ of 24.2°, 33.2°, 35.7°, 40.8°, 49.5°, 54.1°, 57.5°, 62.3°, 64.0°, 71.9° and 75.4° (Geng et al., 2012; Wu et al., 2013; Moyseowicz et al., 2017). The deposited film is definitely well-crystallized due to sharp feature of the reflexes. Besides that, broad signals located at 2Θ of c.a. 26° and 44° can be seen in this diffractogram, that are characteristic for carbon cloth
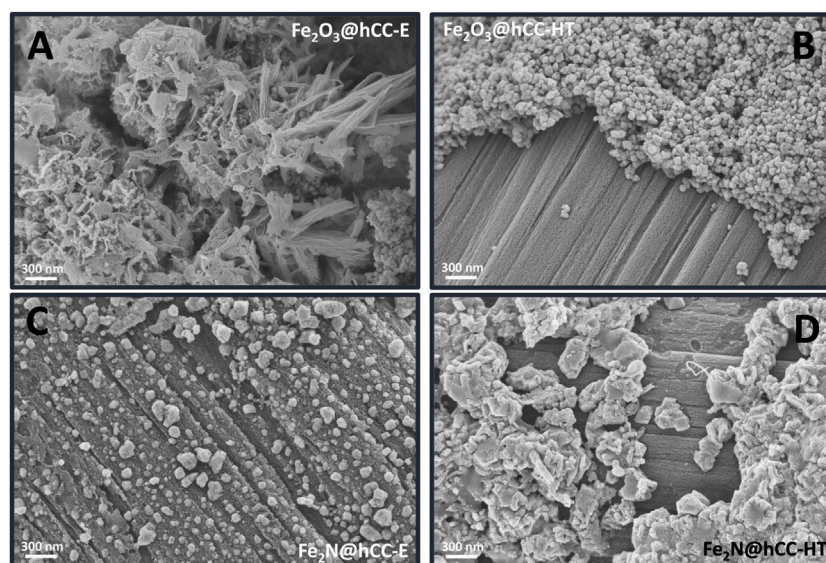
**FIGURE 1**
SEM images of iron oxides and iron nitrides materials on a carbon cloth prepared by hydrothermal and electrodeposition techniques.
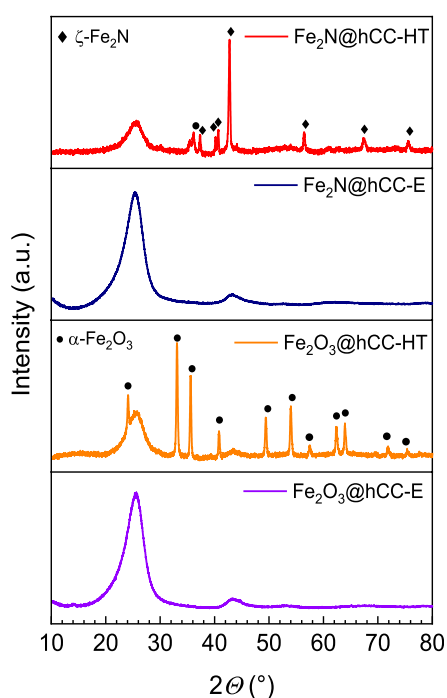


**FIGURE 2**
XRD patterns of the iron oxides and iron nitrides materials prepared by hydrothermal and electrodeposition techniques.

**TABLE 1** Surface atomic concentrations of elements in nitride and oxide samples prepared by hydrothermal and electrodeposition techniques.

| Sample | Surface concentration of elements [at.%] | | | |
|---|---|---|---|---|
|  | Fe | O | C | N |
| $Fe_2N@hCC-HT$ | 8.5 | 19.4 | 70.6 | 1.4 |
| $Fe_2N@hCC-E$ | 3.7 | 7.2 | 87.8 | 1.3 |
| $Fe_2O_3@hCC-HT$ | 20.4 | 38.0 | 41.7 | --- |
| $Fe_2O_3@hCC-E$ | 6.6 | 13.3 | 80.1 | --- |

(Walendzik et al., 2023). The nitridation of the $Fe_2O_3@hCC-HT$ sample also resulted in the formation of well-crystallized product. Diffractogram of $Fe_2N@hCC-HT$ shows, besides signals derived from carbon cloth, a diffraction pattern typical for $\zeta$-$Fe_2N$ phase (JCPDS 50–0958), with reflexes located at $2\Theta$ of 35.4°, 37.4°, 40.1°, 40.9°, 43.0°, 56.9°, 68.1° and 76.0° (Śliwak et al., 2017). The narrow width of the reflexes suggests the big nitride crystallite size. On the other hand, diffractograms of both samples prepared with aid of electrodeposition technique are very different from those of materials prepared hydrothermally. Despite the presence of the thick electrodeposited film in the $Fe_2O_3@hCC-E$ sample (as evidenced by SEM), diffractogram of this sample has only signals that can be attributed to carbon cloth. This leads to the conclusion that the deposited film is amorphous or sub-nanocrystalline (Valvoda, 1996). What is more, an iron nitride ($Fe_2N@hCC-E$) formed upon amination of this sample shows similar diffractogram, therefore the nanoparticles that can be seen in its SEM image are also of amorphous structure.

In order to further characterize the chemical states of elements on the surfaces of the 4 electrodes, XPS technique was applied. As can be noticed in Table 1, iron is present in all samples, indicating that in all samples, iron-based films are formed. The iron concentration in the samples obtained by hydrothermal treatment is evidently higher than in electrodeposited materials, suggesting that more active material was deposited by the former technique. Fe/O atomic ratio for both samples with iron oxide films is similar (0.54 and 0.49 for hydrothermal and electrodeposition
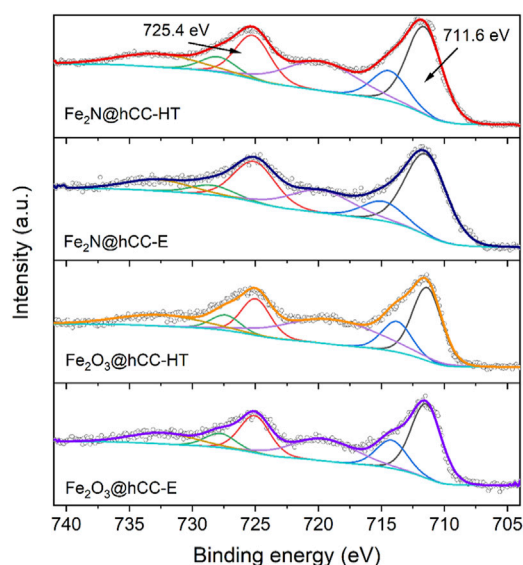
**FIGURE 3**
High-resolution XPS spectra in Fe 2p region of the iron oxides and iron nitrides materials prepared by hydrothermal and electrodeposition techniques.
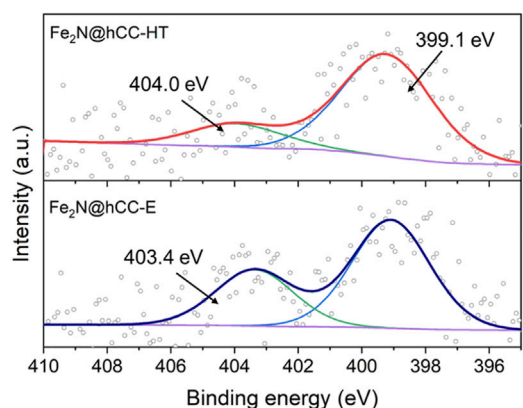


**FIGURE 5**
Bright-field **(A,C)** and high-resolution TEM images **(B,D)** for the Fe$_2$N@hCC samples.



**FIGURE 4**
High-resolution XPS spectra in N 1s region of the iron nitrides materials prepared by hydrothermal and electrodeposition techniques.

techniques, respectively), indicating similar surface chemical states of both oxides.

Similar atomic concentrations of nitrogen can be found in both samples obtained after nitridation. For both samples Fe/N ratio (of 6.1 for Fe$_2$N@hCC-HT and 2.8 for Fe$_2$N@hCC-E) is higher than stoichiometric for Fe$_2$N (2) suggesting that in both materials iron can partially be found in the surface in different form. It is possible that upon the thermal treatment, iron nitride with lower nitrogen content was formed (Park et al., 2016). It can be pointed out here, that metal nitrides usually undergo surface oxidation with the formation of metal oxides (Dong et al., 2017).
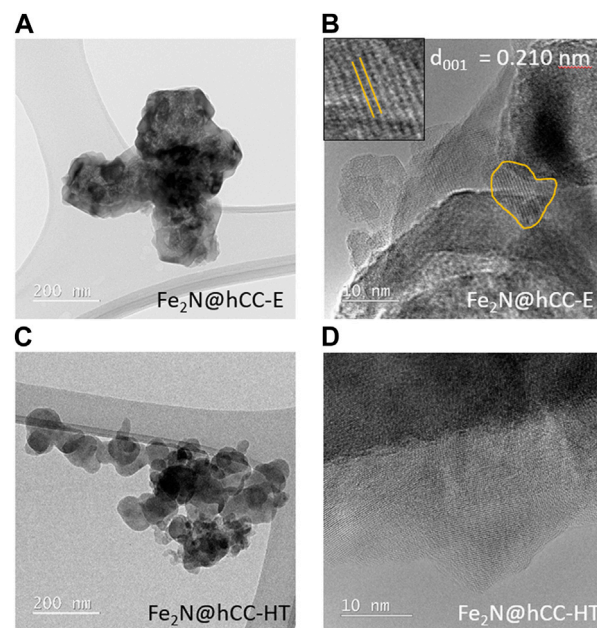
Furthermore, high resolution XPS spectra in the Fe 2p and N 1s regions are presented in Figure 3 and Figure 4. In all spectra distinct Fe 2p$_{3/2}$ and Fe 2p$_{1/2}$ peaks can be seen at binding energies of 711.6 and 725.4 eV, respectively, that are characteristic for α-Fe$_2$O$_3$ phase. Typical for this phase are also the satellite features located at binding energies of 719.5 and 733.0 eV (Cao et al., 2015; Yan et al., 2017). The fact that both oxide and nitride materials possess nearly identical XPS spectra in the Fe 2p region can be explained by the oxidation of surface Fe$_2$N with the formation of thin Fe$_2$O$_3$ layer. XPS is a surface sensitive technique which analyzes only a few atomic monolayers, so majority of the signal comes from this oxidized layer. Surface oxidation of Fe$_2$N into oxide phase was widely discussed in the literature (Dong et al., 2017). As oxidized layer is very thin, therefore its diffraction reflexes cannot be distinguished in XRD patterns of nitride samples.

High resolution N 1s spectra are presented in Figure 4 for both nitride samples. The spectra can be deconvoluted into two peaks. In both spectra, the most intensive component is located at the binding energy of 399.1 eV and can be attributed to metal-nitrogen bonds or pyridinic N, as their binding energy values are almost the same (Wu et al., 2011; Peng et al., 2013; Yu et al., 2018; Kohila Rani et al., 2020). The other peak can be distinguished at 404.0 and 403.4 eV for Fe$_2$N@hCC-HT and Fe$_2$N@hCC-E, respectively. Signals in this spectral region (between 403 and 406 eV) are usually attained to nitrogen-oxygen bonds (Arrigo et al., 2010; Kordek-Khalil et al., 2022). Characterizations of all samples show that the two nitride samples are both composed of Fe$_2$N phase covered by thin Fe$_2$O$_3$ layer generated by atmospheric oxidation of the nitrides. What differs between the samples is the film morphology as well as structure, which in the case of the sample prepared by hydrothermal technique is crystalline with distinct XRD reflexes
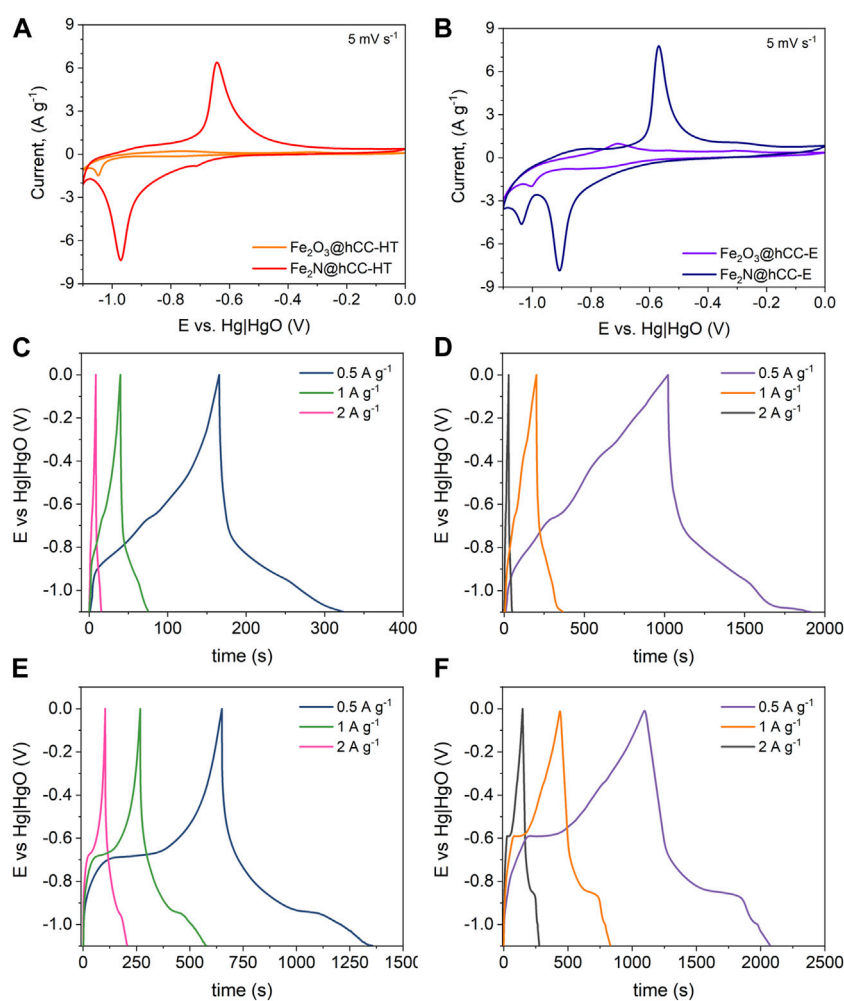
**FIGURE 6**
Electrochemical measurements results from a three-electrode cell: CV curves at a scan rate of 5 mV s$^{-1}$ **(A,B)** and GCD profiles at different current densities of the Fe$_2$O$_3$@hCC-HT **(C)**, Fe$_2$O$_3$@hCC-E **(D)**, Fe$_2$N@hCC-HT **(E)** and Fe$_2$N@hCC-E **(F)**.

and is amorphous for the electrodeposited film. Similar is the case with source metal oxides, which also possess similar surface characteristics but differ in morphology and structure. In general, electrodeposition leads to the formation of amorphous films, and the hydrothermal method forms well-crystallized nanocrystalline products.

Figure 5 presents HRTEM images of the samples after the nitridation procedure. As can be seen in the bright-field images, the Fe$_2$N@hCC-HT sample is composed of smaller nanoparticles than Fe$_2$N@hCC-E, which is consistent with SEM images. Furthermore, high-resolution TEM images of the samples were also acquired to get an insight into the structure of the materials. As can be seen in Figure 5B, the sample Fe$_2$N@hCC-E possesses small crystalline domains (with a diameter of ca. 10 nm) in a rather amorphous matrix. The interplanar distance of 0.210 nm in these domains corresponds to the (011) crystalline plane of hexagonal Fe$_2$N (Jiang et al., 2019), which is also confirmed by the SAED ring (Supplementary Figure S1). On the other hand, Fe$_2$N@hCC-HT sample is evidently more crystalline with a fringe spacing of 0.25 nm (Figure 5D) and can be attributed to Fe$_2$O$_3$, which based on XPS

results, is a product of surface oxidation of Fe$_2$N (Chen et al., 2016). Additionally, the SAED ring patterns also implies the Fe$_2$O$_3$ presence on the surface of the Fe$_2$N@hCC-HT (Supplementary Figure S1).

Figure 6 displays the findings of the CV measurements, which reveal distinct differences in the electrochemical behavior between iron oxides and iron nitrides, as well as comparision between materials from electrodeposition and hydrothermal/drop casting method. The iron-based compounds exhibit clear redox peaks when a lower cutoff potential is used (i.e., below −1.0 V vs. Hg|HgO). The Fe$_2$O$_3$@hCC-HT electrode shows poor electrochemical behavior (Figure 6A), with a very weak peaks of an Fe$^{3+}$ ⇆ Fe$^{2+}$ redox pair and a small peak related to Fe$^{2+}$ reduction to metallic Fe$^0$ at a potential of −1.05 V vs. Hg|HgO electrode (Zhang et al., 2016). However, the Fe$_2$O$_3$ obtained from the electrodeposition process presents improved electrochemical performance compared to its hydrothermal counterpart (Figure 6B). The CV curve of Fe$_2$O$_3$@hCC-E shows the cathodic peak attributed to Fe$^{2+}$ reduction to metallic Fe$^0$, however due to its nanosheet-like morphology, the additional peak appeared at −0.71 V vs. Hg|HgO electrode, related
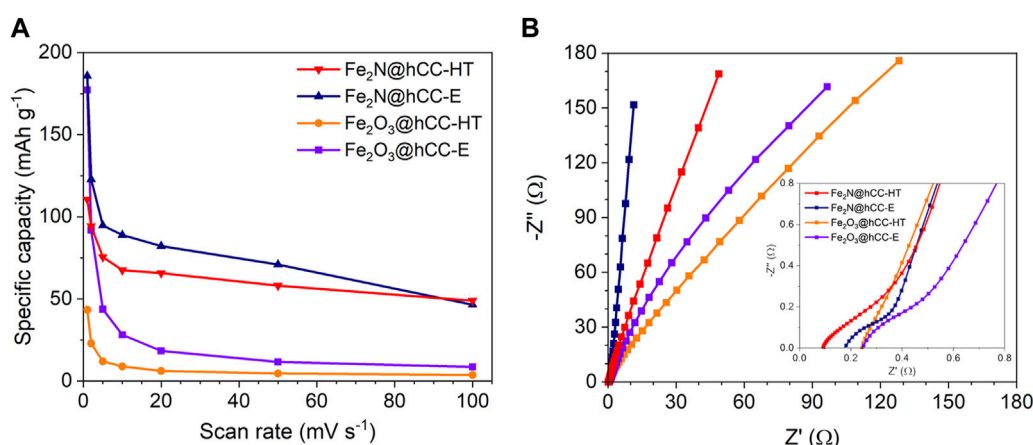
**FIGURE 7**
Specific capacity versus scan rate **(A)** and Nyquist plots with an inset representing the high-frequency region **(B)** of the iron oxides and iron nitrides materials prepared by hydrothermal and electrodeposition techniques.

to the conversion of the intermediate phase of adsorbed iron hydroxide to $Fe^{2+}$ (Li et al., 2015). The effect of a high temperature nitridation of the $Fe_2O_3$@hCC electrodes is very pronounced and greatly improves the electrochemical response of converted iron oxides to nitrides. Due to the increase in conductivity of the $Fe_2N$ form, the CV profile of the $Fe_2N$@hCC-HT presents distinct redox pair related to the transition of $Fe^{3+}$ to $Fe^{2+}$ at the potentials value of −0.97 V vs. Hg|HgO for cathodic and −0.64 V vs. Hg|HgO for anodic peak (Xu et al., 2017; Zhao et al., 2023), therefore indicating a battery-type behavior of the $Fe_2N$ in an alkaline electrolyte. Furthermore, the CV curve revealed that during electrochemical measurement, the $Fe_2N$@hCC-E sample undergoes further reduction to metallic iron, showing a peak above 1.0 V vs. Hg|HgO, which may influence a $Fe^{3+} \leftrightarrows Fe^{2+}$ redox potential, shifting it towards more positive values by 70 mV (Li et al., 2015). Finally, even at a low scan rate of 5 mV s⁻, the peak correlated to the hydrogen evolution reaction is not observed for the $Fe_2N$@hCC samples, due to the increased hydrogen evolution potential of iron nitride (Theerthagiri et al., 2020).

The GCD measurements confirm the results obtained from the CV measurements. The $Fe_2O_3$@hCC electrodes show a distorted, quasi-triangular shape, with an linear part above −0.8 V vs. Hg|HgO, which is mostly related to the charge stored in the $Fe^{2+}$ to $Fe^0$ transition (Figures 6C, D). Moreover, the time required for discharge of the $Fe_2O_3$@hCC-E is over 6 times longer than that of $Fe_2O_3$@hCC-HT at a current density of 0.5 A g⁻¹. The nitridation of the $Fe_2O_3$@hCC electrodes changes significantly the GCD profiles, as visible plateaus are observed, which correspond to the redox peaks of cyclic voltammograms at −0.71 ÷ −0.64 V and −1.05 ÷ −0.97 V vs. Hg|HgO (Figures 6E, F), thus confirming the $Fe_2N$ battery-like electrochemical behavior (Simon et al., 2014; Xu et al., 2017).

The relationships between the specific capacity and scan rate are presented in Figure 7A. The highest specific capacity at a scan rate of 1 mV s⁻¹ is achieved by the $Fe_2N$@hCC-E sample, with a value of 186 mAh g⁻¹, followed by $Fe_2O_3$@hCC-E (177 mAh g⁻¹), showing the superiority of the electrodeposition method over the hydrothermal synthesis combined with drop casting technique. The specific capacity of $Fe_2N$@hCC-HT was 112 mAh g⁻¹, 66% less than its counterpart from the electrodeposition procedure, while the lowest specific capacity value of 43 mAh g⁻¹ was measured for $Fe_2O_3$@hCC-HT sample. Furthermore, from the discharge time of the GCD profiles, the specific capacity values ($Q_s$) can be calculated, accordingly to the Equation 2 and at a current density of 0.5 A g⁻¹ the $Q_s$ were 22, 126, 98 and 135 mAh g⁻¹, $Fe_2O_3$@hCC-HT, $Fe_2O_3$@hCC-E, $Fe_2N$@hCC-HT and $Fe_2N$@hCC-E, respectively, corresponding to the performance between 2 and 5 mV s⁻¹ from the CV measurements. The aggregated, spherical-like morphology does not provide enough active sites for redox reactions; thus, iron-based films from hydrothermal treatment have lower charge storage capability. Moreover, the small nanoparticle size of a thin iron nitride film in the $Fe_2N$@hCC-E sample and the amorphous nature of the iron oxide precursor led to the improved electrochemical response (Zhang et al., 2016; Eftekhari and Mohamedi, 2017). Under increasing scan rate up to 100 mV s⁻¹, the $Fe_2N$@hCC electrodes show over 5-times higher specific capacity than their $Fe_2O_3$ precursors.

The electrochemically active surface areas of the samples do not directly correlate with material activities as supercapacitor electrodes (Supplementary Figure S2). In general, the areas of electrodes fabricated using electrodeposition are higher than those of the samples prepared by the hydrothermal technique. Furthermore, as can be seen the nitridation of electrodeposited film results in decrease of electrochemically active surface while the effect is reverse for hydrothermal materials. This is consistent with the SEM images that show material shrinking in case of electrodeposited electrode and particles growth in case of hydrothermally obtained films. The limited electrochemically active surface area seen in the $Fe_2O_3$@hCC-HT electrode may be attributed to the nanoscale dimensions of its particles, which could potentially lead to a lack of electrical contact between some nanoparticles and the hCC electrode.

EIS measurements were performed to gain further insight into the electrochemical characteristics of the synthesized materials, and the results are presented in the form of a Nyquist plots (Figure 7B). Supplementary Figure S3 presents the fitted equivalet circuit which consists of bulk resistance ($R_b$), a constant phase elements (CPE),

resistance related to surface porosity ($R_p$), a charge transfer resistance ($R_{ct}$) and the Warburg impedance (Wu et al., 2021). The joint electrolyte resistance and current collector resistance defined as bulk resistance ($R_b$), determined from the intersection of the $Z'$ were 0.09, 0.18 and 0.25 $\Omega$ for Fe$_2$N@hCC-HT, Fe$_2$N@hCC-E and both Fe$_2$O$_3$@hCC, respectively (Gajewska et al., 2023). The $R_p$ values were 0.23, 0.19, 0.61 and 58.4 $\Omega$ for Fe$_2$N@hCC-HT, Fe$_2$N@hCC-E, Fe$_2$O$_3$@hCC-E and Fe$_2$O$_3$@hCC-HT, respectively, suggesting improved conductivity within iron-based films obtained from electrodeposition technique. No distinct semicircle in the high-frequency range of the Nyquist plots was observed, which suggests minimized resistance between the binder-free electrode made of iron compounds deposited at the hCC and a current collector (Allison and Andreas, 2019). The charge transfer resistance $R_{ct}$ was significantly lower for iron nitrides than their Fe$_2$O$_3$ counterparts, which implies that nitrides exhibit much faster electron transfer during the electrochemical reaction (Fe$_2$N@hCC-HT (0.22 $\Omega$) vs. Fe$_2$O$_3$@hCC-HT (0.41 $\Omega$) and Fe$_2$N@hCC-E (0.05 $\Omega$) vs. Fe$_2$O$_3$@hCC-E (0.21 $\Omega$)) (Jiang et al., 2016). Next, a straight 45° line indicates the presence of Warburg impedance, which corresponds to diffuse layer resistance, and then in the low-frequency region, the more inclined the plot is towards the -$Z''$ axis, the lower the resistance related to the equilibrium differential capacitance. Among all tested samples, Fe$_2$N@hCC-E exhibits the most vertical line, confirming the formation of an electric double layer at the electrode/electrolyte interface, further indicating a good electric charge storage performance (Mei et al., 2018; Zhao et al., 2023). The EIS data is in good agreement with the CV and GCD measurements, showing that Fe$_2$N exhibits better electrochemical performance than Fe$_2$O$_3$, an additionally confirming that the electrodeposition method for iron nitride precursor is more efficient and promising approach than hydrothermal and drop casting methods.

The long-term performance of the electrode material is another factor in the evaluation of its applicability in energy storage devices. The results of the cyclic stability tests for 2000 cycles at a current density of 1 A g$^{-1}$ are presented in Supplementary Figure S4. While the long-term performance of the Fe$_2$N@hCC electrodes from both preparation methods is very close, the Fe$_2$O$_3$-based electrodes show significant discrepancies, emphasizing the superiority of the electrodeposition method over the hydrothermal/drop casting technique. The highest capacity retention was observed for Fe$_2$O$_3$@hCC-E (65%), followed by Fe$_2$N@hCC-E (61%), Fe$_2$N@hCC-E (56%), and Fe$_2$O$_3$@hCC-HT (36%). The trend is similar to the results of the electrochemically active surface area, where materials for electrodeposition exhibit a higher surface accessible for EDL charge storage, resulting in slower electrochemical dissolution of Fe-based compounds (Wang et al., 2021).

## 4 Conclusion

This work presents a study on the influence of the synthesis protocol of Fe$_2$O$_3$ films deposited on carbon cloth, which are the precursors for Fe$_2$N on carbon cloth binder-free electrodes. The results of the as-prepared iron-based electrodes show that electrodeposition and hydrothermal/drop casting techniques both before and after nitridation reveal distinct differences between the two methods. Hydrothermal synthesis yields highly crystalline α-Fe$_2$O$_3$, while XRD diffraction patterns show that from the direct electrodeposition, amorphous Fe$_2$O$_3$ interconnected nanosheets are present on the

surface of a carbon cloth. XPS studies revealed a superficial oxidation of the Fe$_2$N to Fe$_2$O$_3$ due to the exposure to air. The study demonstrates that both iron oxide and iron nitride from the electrodeposition synthesis exhibit different and superior electrochemical behavior and performance compared to their hydrothermal counterparts. The Fe$_2$N@hCC-E sample exhibits the highest specific capacity at a scan rate of 1 mV s$^{-1}$, with a value of 186 mAh g$^{-1}$. The obtained results show promising potential for the optimization and application of Fe$_2$N@hCC from combined electrodeposition and nitridation protocols as a binder-free negative electrode for hybrid supercapacitors.

## Data availability statement

The raw data supporting the conclusion of this article will be made available by the authors, without undue reservation.

## Author contributions

KK-K: Conceptualization, Formal Analysis, Investigation, Methodology, Writing–original draft. AM: Formal Analysis, Investigation, Methodology, Writing–original draft. AKM: Conceptualization, Funding acquisition, Investigation, Supervision, Writing–review and editing.

## Funding

## Conflict of interest

The authors declare that the research was conducted in the absence of any commercial or financial relationships that could be construed as a potential conflict of interest.

## Publisher's note

All claims expressed in this article are solely those of the authors and do not necessarily represent those of their affiliated organizations, or those of the publisher, the editors and the reviewers. Any product that may be evaluated in this article, or claim that may be made by its manufacturer, is not guaranteed or endorsed by the publisher.

## Supplementary material

The Supplementary Material for this article can be found online at: https://www.frontiersin.org/articles/10.3389/fmats.2023.1273628/full#supplementary-material

# References

Adalati, R., Sharma, M., Sharma, S., Kumar, A., Malik, G., Boukherroub, R., et al. (2022). Metal nitrides as efficient electrode material for supercapacitors: A review. *J. Energy Storage* 56, 105912. doi:10.1016/J.EST.2022.105912

Allison, A., and Andreas, H. A. (2019). Minimizing the Nyquist-plot semi-circle of pseudocapacitive manganese oxides through modification of the oxide-substrate interface resistance. *J. Power Sources* 426, 93–96. doi:10.1016/J.JPOWSOUR.2019.04.029

Arrigo, R., Hävecker, M., Wrabetz, S., Blume, R., Lerch, M., McGregor, J., et al. (2010). Tuning the acid/base properties of nanocarbons by functionalization via amination. *J. Am. Chem. Soc.* 132, 9616–9630. doi:10.1021/ja910169v

Augustyn, V., Simon, P., and Dunn, B. (2014). Pseudocapacitive oxide materials for high-rate electrochemical energy storage. *Energy Environ. Sci.* 7, 1597–1614. doi:10.1039/c3ee44164d

Borenstein, A., Hanna, O., Attias, R., Luski, S., Brousse, T., and Aurbach, D. (2017). Carbon-based composite materials for supercapacitor electrodes: a review. *J. Mat. Chem. A* 5, 12653–12672. doi:10.1039/C7TA00863E

Cao, K., Jiao, L., Liu, H., Liu, Y., Wang, Y., Guo, Z., et al. (2015). 3D hierarchical porous α-Fe₂O₃ nanosheets for high-performance lithium-ion batteries. *Adv. Energy Mater* 5. doi:10.1002/AENM.201401421

Chen, D., Zhou, S., Quan, H., Zou, R., Gao, W., Luo, X., et al. (2018). Tetsubo-like α-Fe₂O₃/C nanoarrays on carbon cloth as negative electrode for high-performance asymmetric supercapacitors. *Chem. Eng. J.* 341, 102–111. doi:10.1016/J.CEJ.2018.02.021

Chen, M., Zhao, E., Yan, Q., Hu, Z., Xiao, X., and Chen, D. (2016). The effect of crystal face of Fe₂O₃ on the electrochemical performance for lithium-ion batteries. *Sci. Rep.* 6, 1–9. doi:10.1038/srep29381

Cherusseri, J., Sambath Kumar, K., Choudhary, N., Nagaiah, N., Jung, Y., Roy, T., et al. (2019). Novel mesoporous electrode materials for symmetric, asymmetric and hybrid supercapacitors. *Nanotechnology* 30, 202001. doi:10.1088/1361-6528/AB0685

Chi, H. Z., Wu, Y. Q., Shen, Y. K., Zhang, C., Xiong, Q., and Qin, H. (2018). Electrodepositing manganese oxide into a graphene hydrogel to fabricate an asymmetric supercapacitor. *Electrochim Acta* 289, 158–167. doi:10.1016/J.ELECTACTA.2018.09.025

Dong, Y., Wang, B., Zhao, K., Yu, Y., Wang, X., Mai, L., et al. (2017). Air-stable porous Fe₂N encapsulated in carbon microboxes with high volumetric lithium storage capacity and a long cycle life. *Nano Lett.* 17, 5740–5746. doi:10.1021/ACS.NANOLETT.7B02698

Dubal, D. P., Ayyad, O., Ruiz, V., and Gómez-Romero, P. (2015). Hybrid energy storage: the merging of battery and supercapacitor chemistries. *Chem. Soc. Rev.* 44, 1777–1790. doi:10.1039/c4cs00266k

Eftekhari, A., and Mohamedi, M. (2017). Tailoring pseudocapacitive materials from a mechanistic perspective. *Mater Today Energy* 6, 211–229. doi:10.1016/j.mtener.2017.10.009

Feng, T., Liu, G., Li, G., Li, Y., Liang, J., and Wang, K. (2023). Engineering iron-rich nanomaterials for supercapacitors. *Chem. Eng. J.* 2023, 145045. doi:10.1016/J.CEJ.2023.145045

Gajewska, K., Moyseowicz, A., Minta, D., Zyna Gryglewicz, G., and Sci, J. M. (2023). Effect of electrolyte and carbon material on the electrochemical performance of high-voltage aqueous symmetric supercapacitors. *J. Mater. Sci.* 2023, 1. doi:10.1007/S10853-023-08148-5

Geng, B., Tao, B., Li, X., and Wei, W. (2012). Ni²⁺/surfactant-assisted route to porous α-Fe₂O₃ nanoarchitectures. *Nanoscale* 4, 1671. doi:10.1039/c2nr12102f

Gong, S. G., Shi, Y. H., Su, Y., Li, Y. F., Ding, L., Lin, J., et al. (2021). *In situ* growth of 3D lamellar Mn(OH)₂on CuO-coated carbon cloth for flexible Asymmetric supercapacitors with a high working voltage of 2.4 v. *ACS Sustain Chem. Eng.* 9, 13385–13394. doi:10.1021/ACSSUSCHEMENG.1C05164

Idrees, M., Mukhtar, A., Ata-ur-Rehman, Abbas, S. M., Zhang, Q., and Li, X. (2021). Transition metal nitride electrodes as future energy storage devices: A review. *Mater Today Commun.* 27, 102363. doi:10.1016/J.MTCOMM.2021.102363

Jiang, H., Huang, L., Wei, Y., Wang, B., Wu, H., Zhang, Y., et al. (2019). Bio-derived hierarchical multicore–shell Fe₂N-Nanoparticle-Impregnated N-doped carbon nanofiber bundles: A host material for lithium-/potassium-ion storage. *Nanomicro Lett.* 11, 1–17. doi:10.1007/S40820-019-0290-0/FIGURES/7

Jiang, M., Li, Y., Lu, Z., Sun, X., and Duan, X. (2016). Binary nickel–iron nitride nanoarrays as bifunctional electrocatalysts for overall water splitting. *Inorg. Chem. Front.* 3, 630–634. doi:10.1039/C5QI00232J

Jin, W. H., Cao, G. T., and Sun, J. Y. (2008). Hybrid supercapacitor based on MnO₂ and columned FeOOH using Li₂SO₄ electrolyte solution. *J. Power Sources* 175, 686–691. doi:10.1016/J.JPOWSOUR.2007.08.115

Kohila Rani, K., Karuppiah, C., Wang, S. F., Alaswad, S. O., Sireesha, P., Devasenathipathy, R., et al. (2020). Direct pyrolysis and ultrasound assisted preparation of N, S co-doped graphene/Fe₃C nanocomposite as an efficient electrocatalyst for oxygen reduction and oxygen evolution reactions. *Ultrason. Sonochem.* 66, 105111. doi:10.1016/J.ULTSONCH.2020.105111

Kordek, K., Jiang, L., Fan, K., Zhu, Z., Xu, L., Al-Mamun, M., et al. (2019). Two-step Activated carbon cloth with oxygen-rich functional groups as a high-performance additive-free Air electrode for flexible zinc–Air batteries. *Adv. Energy Mater* 9, 1802936. doi:10.1002/AENM.201802936

Kordek-Khalil, K., Walendzik, I., and Rutkowski, P. (2022). Low-overpotential full water splitting with metal-free self-supported electrodes obtained by amination of oxidised carbon cloth. *Sustain. Energy Technol. Assessments* 53, 102569. doi:10.1016/J.SETA.2022.102569

Li, R., Wang, Y., Zhou, C., Wang, C., Ba, X., Li, Y., et al. (2015). Carbon-stabilized high-capacity ferroferric oxide nanorod array for flexible solid-state Alkaline battery–supercapacitor hybrid device with high environmental suitability. *Adv. Funct. Mater* 25, 5384–5394. doi:10.1002/ADFM.201502265

Mei, B. A., Munteshari, O., Lau, J., Dunn, B., and Pilon, L. (2018). Physical interpretations of nyquist plots for EDLC electrodes and devices. *J. Phys. Chem. C* 122, 194–206. doi:10.1021/ACS.JPCC.7B10582

Moyseowicz, A., Gryglewicz, S., and Gryglewicz, G. (2021). Enhancing electrochemical capacitor performance through the application of nanostructured carbon materials as conducting additives. *Chem. Eng. Process. - Process Intensif.* 169. doi:10.1016/j.cep.2021.108647

Moyseowicz, A., and Moyseowicz, A. (2021). One-pot synthesis of bismuth sulfide nanostructures as an active electrode material for aqueous hybrid capacitors. *Energies (Basel)* 14, 2670. doi:10.3390/EN14092670/S1

Moyseowicz, A. (2019). Scalable one-pot synthesis of bismuth sulfide nanorods as an electrode active material for energy storage applications. *J. Solid State Electrochem.* 23, 1191–1199. doi:10.1007/s10008-019-04215-7

Moyseowicz, A., Śliwak, A., Miniach, E., and Gryglewicz, G. (2017). Polypyrrole/iron oxide/reduced graphene oxide ternary composite as a binderless electrode material with high cyclic stability for supercapacitors. *Compos B Eng.* 109, 23–29. doi:10.1016/j.compositesb.2016.10.036

Park, M. J., Lee, J. H., Hembram, K. P. S. S., Lee, K. R., Han, S. S., Yoon, C. W., et al. (2016). Oxygen reduction electrocatalysts based on coupled iron nitride nanoparticles with nitrogen-doped carbon. *Catalysts* 6, 86. doi:10.3390/CATAL6060086

Peng, H., Mo, Z., Liao, S., Liang, H., Yang, L., Luo, F., et al. (2013). High performance Fe- and N- doped carbon catalyst with graphene structure for oxygen reduction. *Sci. Rep.* 3, 1–7. doi:10.1038/srep01765

Simon, P., Gogotsi, Y., and Dunn, B. (2014). Where do batteries end and supercapacitors begin? *Science* 343, 1210–1211. doi:10.1126/SCIENCE.1249625

Śliwak, A., Moyseowicz, A., and Gryglewicz, G. (2017). Hydrothermal-assisted synthesis of an iron nitride-carbon composite as a novel electrode material for supercapacitors. *J. Mater Chem. A Mater* 5, 5680–5684. doi:10.1039/C6TA10985C

Theerthagiri, J., Lee, S. J., Murthy, A. P., Madhavan, J., and Choi, M. Y. (2020). Fundamental aspects and recent advances in transition metal nitrides as electrocatalysts for hydrogen evolution reaction: A review. *Curr. Opin. Solid State Mater Sci.* 24, 100805. doi:10.1016/J.COSSMS.2020.100805

Valvoda, V. (1996). *About Some Practical Aspects Of X-Ray Diffraction: From Powder To Thin Film.* LNF-IR-96-049.

Walendzik, I., Kordek-Khalil, K., and Rutkowski, P. (2023). Quick-to-synthesize hybrid electrodes composed of activated carbon cloth with Co/Fe-based films as bifunctional electrocatalysts for water splitting. *Int. J. Hydrogen Energy* 48, 25741–25754. doi:10.1016/J.IJHYDENE.2023.03.092

Wang, H., Li, J., Li, K., Lin, Y., Chen, J., Gao, L., et al. (2021). Transition metal nitrides for electrochemical energy applications. *Chem. Soc. Rev.* 50, 1354–1390. doi:10.1039/D0CS00415D

Wu, G., Johnston, C. M., MacK, N. H., Artyushkova, K., Ferrandon, M., Nelson, M., et al. (2011). Synthesis–structure–performance correlation for polyaniline–Me–C non-precious metal cathode catalysts for oxygen reduction in fuel cells. *J. Mater Chem.* 21, 11392–11405. doi:10.1039/C0JM03613G

Wu, L., Shi, D., Yan, S., Qiao, W., Zhong, W., and Du, Y. (2021). Iron-doped cobalt nitride nanoparticles (Fe–Co₃N): an efficient electrocatalyst for water oxidation. *Int. J. Hydrogen Energy* 46, 2086–2094. doi:10.1016/J.IJHYDENE.2020.10.089

Wu, W., Hao, R., Liu, F., Su, X., and Hou, Y. (2013). Single-crystalline α-Fe₂O₃ nanostructures: controlled synthesis and high-index plane-enhanced photodegradation by visible light. *J. Mater Chem. A Mater* 1, 6888–6894. doi:10.1039/C3TA10886D

Xu, L., Sun, L., Feng, J., Qi, L., Muhammad, I., Maher, J., et al. (2017). Nanocasting synthesis of an iron nitride-ordered mesopore carbon composite as a novel electrode material for supercapacitors. *RSC Adv.* 7, 44619–44625. doi:10.1039/C7RA08704G

Yadlapalli, R. T., Alla, R. K. R., Kandipati, R., and Kotapati, A. (2022). Super capacitors for energy storage: progress, applications and challenges. *J. Energy Storage* 49, 104194. doi:10.1016/J.EST.2022.104194

Yan, Y., Tang, H., Wu, F., Wang, R., and Pan, M. (2017). One-step self-assembly synthesis α-Fe2O3 with carbon-coated nanoparticles for stabilized and enhanced supercapacitors electrode. *Energies* 10, 1296. doi:10.3390/EN10091296

Yu, Y., Xiao, D., Ma, J., Chen, C., Li, K., Ma, J., et al. (2018). The self-template synthesis of highly efficient hollow structure Fe/N/C electrocatalysts with Fe–N coordination for the oxygen reduction reaction. *RSC Adv.* 8, 24509–24516. doi:10.1039/C8RA03672A

Zhang, Z., Zhang, H., Chen, Y., Li, Z., Li, Y., Luo, T., et al. (2016). Ultrasmall Fe2O3 nanoparticles anchored on three-dimensional hierarchical porous graphene-like networks for high rate capability supercapacitors. *ChemElectroChem* 3, 1820–1826. doi:10.1002/CELC.201600393

Zhao, G., Ning, K., Wei, M., Zhang, L., Han, L., Zhu, G., et al. (2023). Fabrication and enhanced supercapacitive performance of Fe2N@Cotton-based porous carbon fibers as electrode material. *Resour. Chem. Mater.* 2, 277–287. doi:10.1016/J.RECM.2023.07.005

Zhi, M., Xiang, C., Li, J., Li, M., and Wu, N. (2013). Nanostructured carbon-metal oxide composite electrodes for supercapacitors: a review. *Nanoscale* 5, 72–88. doi:10.1039/c2nr32040a

Zhou, Y., Guo, W., and Li, T. (2019). A review on transition metal nitrides as electrode materials for supercapacitors. *Ceram. Int.* 45, 21062–21076. doi:10.1016/J.CERAMINT.2019.07.151